

Nano-imaging the inhibition of breast cancer cell migration by maduramicin via surface charge alteration using scanning ion conductance microscopy

Xinhao Song^{a,d,1}, Yao Song^{b,1}, Mengjuan Lin^a, Moran Wang^b, Tianqi Jia^b, Juan Jin^b, Jingjing Sun^b, Genhua Duan^a, Xiuge Gao^a, Shanxiang Jiang^a, Feng Chen^{b,*}, Ning Gu^{b,c,**}, Dawei Guo^{a,*}

^a Engineering Center of Innovative Veterinary Drugs, Center for Veterinary Drug Research and Evaluation, MOE Joint International Research Laboratory of Animal Health and Food Safety, College of Veterinary Medicine, Nanjing Agricultural University, 1 Weigang, Nanjing 210095, China

^b Key Laboratory for Bio-Electromagnetic Environment and Advanced Medical Theranostics, School of biomedical engineering and informatics, Nanjing Medical University, Nanjing 211166, China

^c Nanjing Key Laboratory for Cardiovascular Information and Health Engineering Medicine, Institute of Clinical Medicine, Nanjing Drum Tower Hospital, Medical School, Nanjing University, Nanjing 210093, China

^d School of Traditional Chinese Pharmacy, China Pharmaceutical University, Nanjing 211100, China

ARTICLE INFO

Keywords:

Scanning ion conductance microscopy
Breast cancer
Maduramicin
Surface charge
Cell migration

ABSTRACT

Cancer cells possess a negatively charged surface that significantly influences key biological processes, including motility and invasiveness. Understanding the cellular membrane at the nanoscale level, especially in deciphering tumor migration mechanisms, is crucial yet complex. In this study, we explored the impact of maduramicin (MAD), a polyether ionophore antibiotic, on the surface charge distribution in tumor cell membranes. Our findings demonstrated that modulating calcium channels and disrupting charge distributions, imaged by a current difference-based scanning ion conductance microscopy (Δ I-SICM) method, resulted in significant reductions in both cell invasiveness and viability. These results emphasize the cell membrane's considerable role at the nano-bio interface, highlighting the intricate relationship between biophysical properties and cellular behaviors. Our research suggests that targeting the charge distribution of cell membrane may offer a novel therapeutic strategy to mitigate cell migration and enhance treatment outcomes in cancer therapy.

Introduction

Breast cancer, originating from mammary epithelial cells, poses a significant global health threat, particularly as its incidence rises with age [1,2]. The diverse cellular phenotypes present in breast cancer complicate detection and therapeutic intervention, emphasizing the necessity for effective early diagnostic and therapeutic strategies [3]. Malignant transformation of tumor cells arises from changes in their physicochemical and biological properties, which include altered morphology, plasticity, apoptosis resistance, proliferative and invasive capabilities, and glycolytic metabolism [4]. Nevertheless, the

substantial modifications in the tumor cell membrane during malignant transformation are often overlooked.

The intrinsic electrical properties of cells crucially govern various cellular functions, including growth, division, specialization, aging, migration, and cell death [4,5]. Variations in electrical properties are essential for disease identification, early detection, and preventive measures [4]. Research indicates that in human tumor cells and tumor blood vessels, exposure to phosphatidylserine and other negatively charged phospholipids leads to increased negative charges. Moreover, studies have identified an overall increase in phospholipid content, alterations in the ratios of phosphatidylcholine and ethanolamine

* Corresponding authors.

** Corresponding author at: Key Laboratory for Bio-Electromagnetic Environment and Advanced Medical Theranostics, School of biomedical engineering and informatics, Nanjing Medical University, Nanjing 211166, China.

E-mail addresses: chenfeng@njmu.edu.cn (F. Chen), guning@nju.edu.cn (N. Gu), gdawei0123@njau.edu.cn (D. Guo).

¹ Xinhao Song⁺ and Yao Song⁺ contributed equally to the work

composition, and anomalies in integrin protein expression levels on cell membranes, during the malignant transformation of tumor cells [6]. Conversely, these negative charges tend to diminish during cell death. Collectively, these factors contribute to an increased net negative charge on tumor cell membranes compared to normal cells, significantly influencing malignant biological processes and tumor signal transduction [7]. Numerous studies have highlighted that the alterations of surface charge can impact membrane-anchored proteins' function, leading to modifications in associated signaling pathways and cascade reactions [6]. However, research on effective interventions to manipulate the surface charge of tumor cell membranes to suppress tumor progression remains limited.

Optical microscopy, encompassing both traditional optical and fluorescence microscopy, is the primary method for characterizing cell morphology. However, due to optical diffraction constraints, achieving high resolution remains challenging. Although confocal microscopy offers superior resolution and facilitates live-cell imaging, it requires staining, which is non-in situ and destructive [8], and does not provide detailed surface information about the cell membrane. As a noncontact scanning probe technology with rapid detection speed and high imaging resolution, scanning ion conductance microscopy (SICM) is well-suited for bio-sample scanning or analyzing, including living cells and tissues, without compromising cellular membranes [9–11]. This innovative approach enables the visualization of the nanoscale structure and functionality of live cells while measuring surface charge distribution [12,13]. The heterogeneity of cell surface charge is integral to essential physiological functions such as electrophysiological signaling, cell growth and division, and particle uptake. Therefore, detecting and visualizing this inhomogeneity can provide valuable insights into

cellular functions [13]. We proposed a synchronous nano-imaging method based on the ionic current difference (ΔI -SICM) technology to examine the membrane topography and charge distribution of human dental pulp stem cells [14]. This ΔI -SICM method offers significant advantages in processing ionic current data, partially mitigating errors in current changes caused by probe blockage during scanning.

In this study, we focus on the impact of maduramicin (MAD), a polyether ionophore antibiotic [15], on modulating and altering the surface charge of tumor cell membranes. Specifically, we aim to determine whether MAD exposure induces changes in the membrane polarity of tumor cells and, if so, whether these alterations influence malignant biological behavior. We hypothesized that modifying tumor cell membranes with MAD would disrupt the interplays between antibiotic and negatively charged membranes, leading to an alteration in surface charge distribution at the nanoscale level. By remodeling membrane polarization, we anticipate a reversal of the malignant behaviors of tumor cells. This study endeavors to utilize an ionophore antibiotic to modulate membrane charge and potentially impede the progression of tumor malignancy.

Results and discussion

Effect of MAD on breast cancer cell proliferation, migration, and invasion in vitro

To investigate the impact of MAD on breast cancers, MDA-MB-231, 4T1, and MCF-7 cells were treated under varying concentrations of MAD for 48 h. The MAD's median inhibitory concentration (IC_{50}) values were found to be $2.50 \pm 0.62 \mu M$ on MDA-MB-231, $2.30 \pm 0.42 \mu M$ on

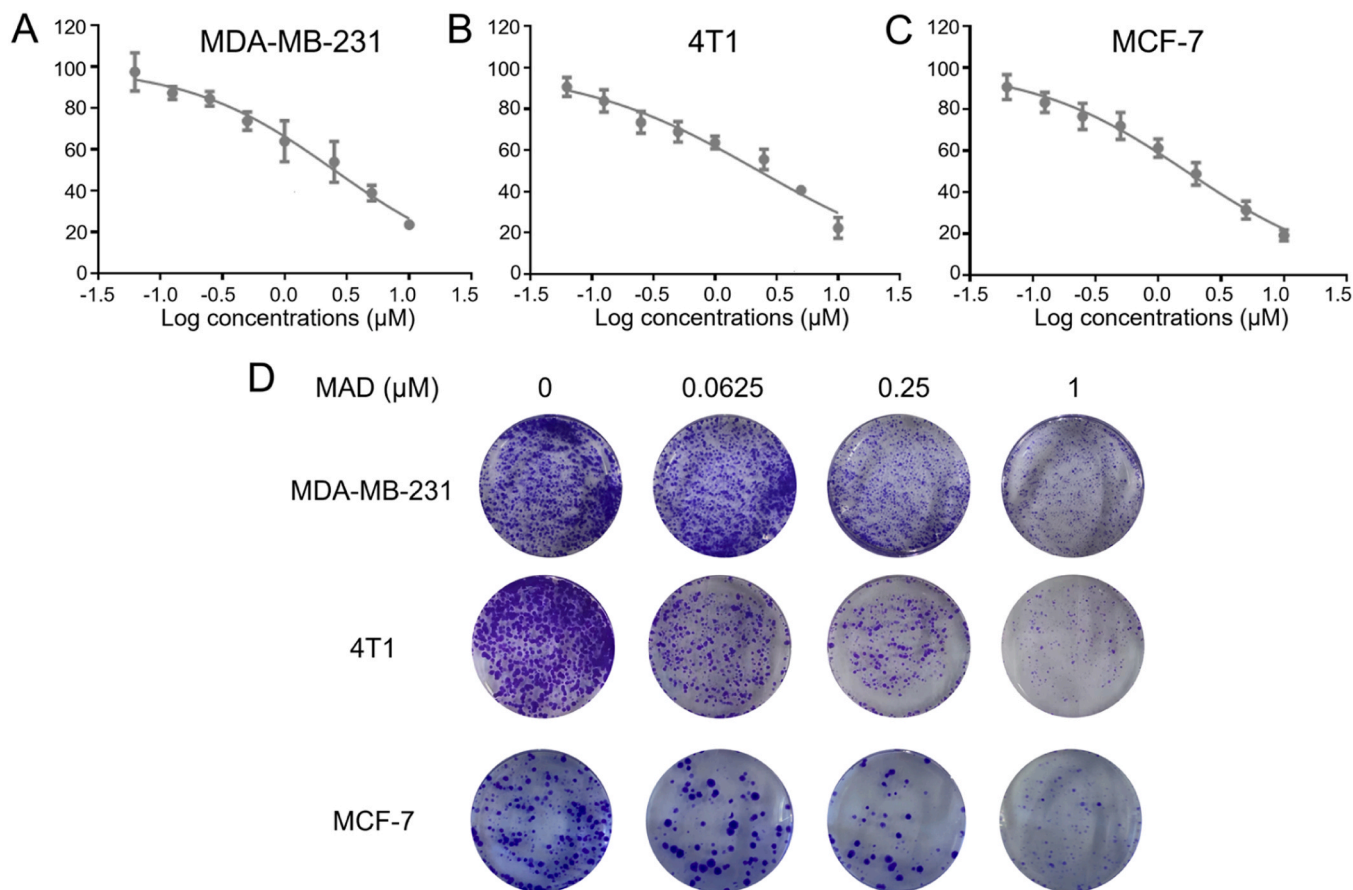


Fig. 1. Effect of MAD on breast cancer cell proliferation. Assessment of cell viability using the CCK-8 assay, showcasing the impact of varying MAD concentrations on MDA-MB-231 (A), 4T1 (B), and MCF-7 (C) cells. (D) Representative images illustrating colony formation across different cancer cell lines treated with various concentrations of MAD.

4T1, and $1.79 \pm 0.32 \mu\text{M}$ on MCF-7 (Table S1). This trend shown in Fig. 1A-C indicated that as the MAD concentration increased, it gradually reduced cell viability, highlighting a potent inhibitory effect on breast cancer cell proliferation. In addition, the survival rate of MCF-10A and EpH4-Ev cells was as high as 71.00 % and 67.36 % at a concentration of $10 \mu\text{M}$, indicating that MAD was less sensitive to normal breast cells (Figure S1). The observed differences in the anti-proliferative effects are primarily attributed to the intrinsic biological variations among these cell lines, encompassing receptor expression, drug metabolism, and genetic backgrounds. This variability is a common phenomenon in oncology, as demonstrated by other drugs [16,17].

Subsequently, colony formation assays were conducted to assess the impact of MAD on the regenerative capacity of these cancer cells (Fig. 1D). The results revealed a significant reduction in colony formation rates across all cells at various MAD concentrations, suggesting that MAD not only inhibits proliferation but also impairs self-renewal capacity. These findings collectively suggest that MAD holds promising anticancer potential.

Tumor metastasis is a critical malignant characteristic of breast cancer that contributes significantly to patient mortality [18,19]. Therefore, effectively inhibiting metastasis is essential for improving survival rates among breast cancer patients. In this study, transwell assays were employed to assess the effect of MAD on the invasion capacity of MDA-MB-231 cells. Results indicated a progressive decline in both migration and invasion with increasing drug concentration, reflecting a dose-dependent relationship (Fig. 2A and B). Additionally, wound-healing assays were carried out to assess the MDA-MB-231 cells' migration ability, revealing significant inhibition of migration with escalating MAD concentrations (Fig. 2C and D). In breast cancer, the epithelial-mesenchymal transition (EMT) phenotype, known to correlate with heightened cell motility, invasion, and metastasis, was investigated. Activation of EMT leads to the downregulation of E-cadherin and the acquisition of mesenchymal characteristics [20,21]. Notably, MAD treatment resulted in the downregulation of N-cadherin and Vimentin expression while upregulating E-cadherin compared with the untreated cells (Fig. 2E). These observations suggest that MAD may

possess a potential anti-migratory effect on breast cancer cells.

Enhancing the efficacy and antimetastatic effect of MAD in vivo

To further evaluate the MAD's potential to inhibit tumor progression *in vivo*, a study was conducted utilizing nude BALB/c mice bearing orthotopic MDA-MB-231 tumors. The mice were orally administrated with either saline or MAD at varying concentrations (0.35, 1.75, and 3.5 mg/kg) every other day for a total of six doses (Fig. 3A). Body weight and tumor volume measurements were recorded every two days, and general clinical observations were conducted daily at 10 AM throughout the experimental period. Regular monitoring of tumor volume and body weight showed that mice in both control and receiving low and moderate MAD doses (0.35 and 1.75 mg/kg) maintained stable health status, with no significant fluctuations in body weight (Fig. 3B). Analysis depicted in Fig. 3C revealed that MAD at the doses of 1.75 and 3.5 mg/kg significantly suppressed breast tumor volume compared to the saline group. Upon euthanasia, tumor tissue collection showed no metastatic lesions in vital organs. Evaluation of tumor weight and volume across groups yielded intriguing results (Fig. 3C-E). The saline group exhibited the highest tumor weight and volume, whereas the group receiving the highest MAD concentration (3.5 mg/kg) displayed the lowest values. MAD-treated groups demonstrated reduced tumor weight and volume compared to the saline group, highlighting MAD's suppressive effect on the tumorigenic potential of MDA-MB-231 cells. Histological staining results (Fig. 3F) highlighted distinct features in the tumor tissues of each group. Untreated tumors consisted of densely packed tumor cells with round and large nuclei, whereas MAD-treated tumors showed characteristics such as coagulative necrosis, empty intercellular spaces, and inhibited cell proliferation. Subsequently, a TUNEL assay was performed to verify the apoptosis of tumor tissues from various groups. The control group exhibited no evident apoptosis, whereas the percentages of apoptotic cells were significantly elevated in MAD-treated groups (Figure S2A). The anti-proliferative effect on tumor cells was further evaluated by Ki67 staining. A decrease in Ki67-positive cells of MAD treatment was shown in Figure S2B, corroborating the tumor

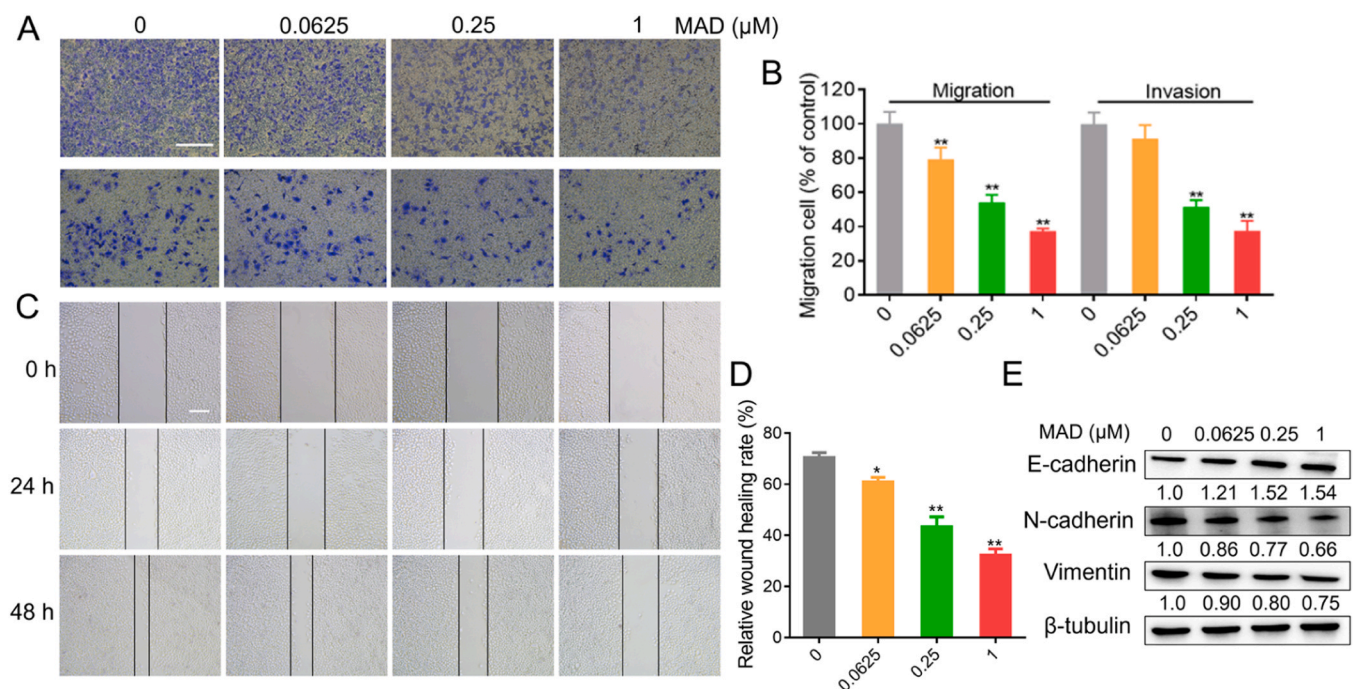


Fig. 2. Influence of MAD on the migration and invasion of MDA-MB-231 cells. (A-B) Transwell assays conducted to evaluate the effects of different MAD concentrations on cell migration and invasion (scale bar: 200 μm). (C-D) Scratch assays performed to assess cell migration (scar bar: 100 μm). (E) Western blot analysis of E-cadherin, N-cadherin, and Vimentin protein expression levels. * $P < 0.05$, ** $P < 0.01$ vs control.

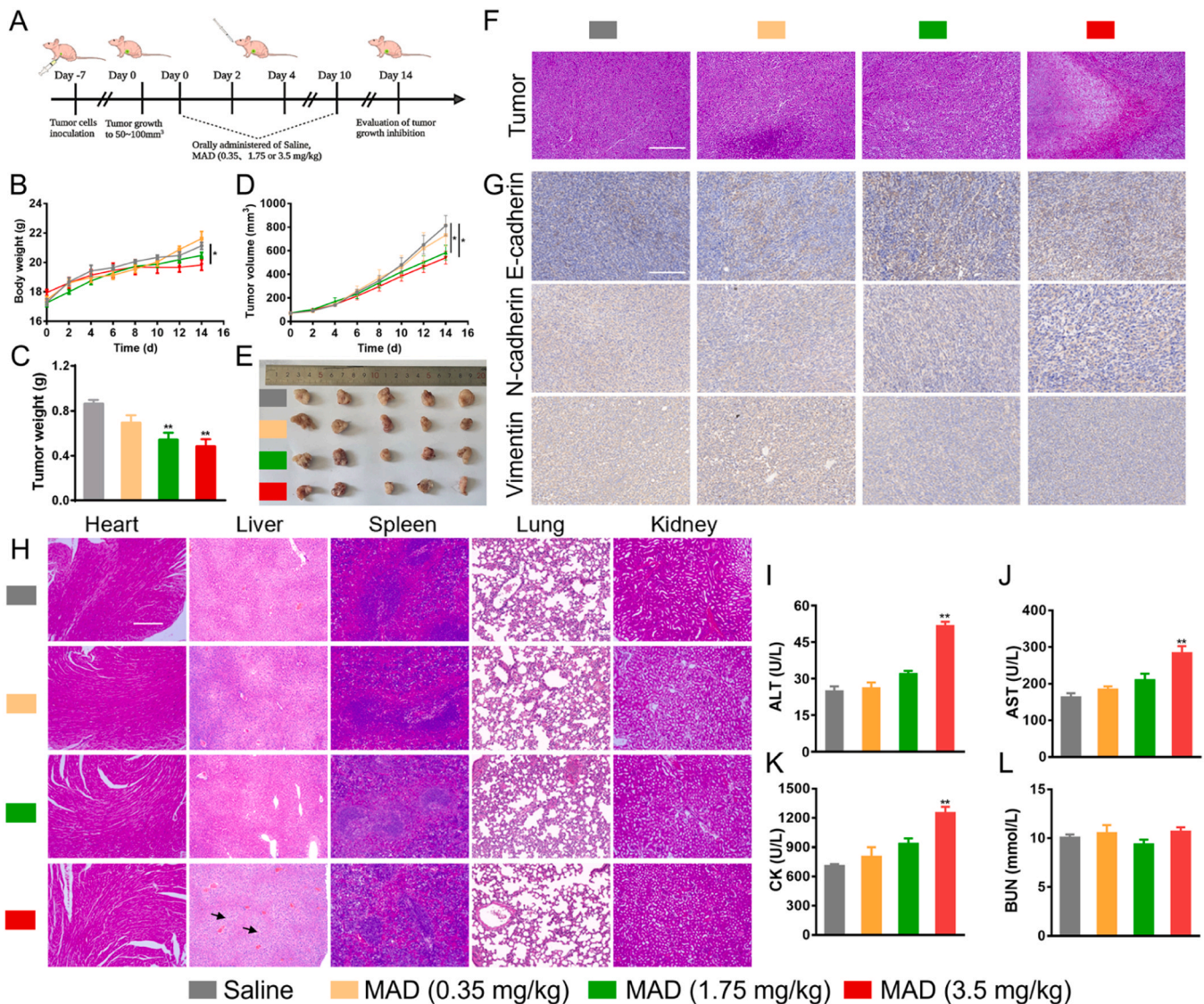


Fig. 3. Antimetastatic efficacy of MAD in nude BALB/c mice bearing orthotopic MDA-MB-231 tumors. (A) Schematic illustration of tumor suppression in mice. MDA-MB-231 cells were injected into the second pair of right mammary glands to establish orthotopic models. Once tumor sizes reached 50–100 mm³, mice were treated with 0.35, 1.75, and 3.5 mg/kg of MAD, with tumor growth inhibition assessed 14 days post-treatment. (B) Monitoring body weight changes following treatment. (C–D) Measurements of tumor weight and volume in tumor-bearing mice after post-treatment. (E) Images showcasing excised tumors from various experimental groups. (F–G) Histopathological (H&E) and immunohistochemical (E-cadherin, Vimentin, and N-cadherin) staining of tumor sections after oral administration (scar bar: 100 μ m). (H) Representative H&E-stained images of primary organs in mice for toxicity assessment (scale bar: 100 μ m). (I–L) Determination of serum creatine kinase (CK), serum aspartate transaminase (AST), alanine transaminase (ALT), and blood urea nitrogen (BUN) levels in mice. * $P < 0.05$, ** $P < 0.01$ vs control.

suppression results. To investigate the anti-metastasis mechanism of MAD, the EMT-related protein expression was evaluated in the tumor tissues. Compared to the saline group, the MAD-treated groups exhibited increased E-cadherin expression and decreased levels of N-cadherin and Vimentin, indicating that MAD could potentially reverse the effect of EMT (Fig. 3G). Overall, these findings suggest that MAD holds promise in inhibiting metastasis *in vivo* context, positioning it as a valuable therapeutic agent.

The histopathological analysis indicated no considerable pathological changes in the organs of mice subjected to saline or those administered with low and medium doses (0.35 and 1.75 mg/kg, respectively). However, mice receiving high-dose treatment (3.5 mg/kg) exhibited mild hepatic and cardiac lesions characterized by tissue vacuolation and disruption of myofibrillar structures, as indicated by the black arrows in Fig. 3H. Additionally, an analysis of blood biochemical indices revealed that all parameters in the saline group remained within the normal physiological range (Fig. 3I–L). In contrast, the high-dose MAD group

demonstrated decreased expressions of alanine aminotransferase (ALT) and aspartate aminotransferase (AST), suggesting hepatic dysfunction. Concurrently, there was an increase in creatine kinase (CK) levels, suggesting potential cardiac injury. Collectively, these results emphasize the antitumor potential of MAD in inhibiting tumor growth and metastasis. Nevertheless, caution is warranted when administering high doses, as it may lead to adverse effects on the liver and heart in nude mice. Higher concentrations in the body enhance the destruction of cancer cells. However, this augmented effect may also harm normal cells, leading to cumulative toxicity in specific organs, such as liver. This highlights the necessity for careful dose optimization and monitoring potential toxicities in future therapeutic applications.

Effectively inhibiting tumor cell pseudopodia extension with MAD

The aggressive invasiveness of tumor cells signifies a crucial malignant trait, facilitated by various mechanisms, including enhanced

motility through pseudopodia formation, cytoskeleton reorganization, integrin protein anchoring, and matrix metalloproteinase secretion[22]. These pathways collectively contribute to extracellular matrix remodeling, thereby amplifying the invasive capability[23]. As illustrated in Fig. 4A and B, an analysis of pseudopod-related gene and protein expression demonstrated that MAD significantly impeded tumor cell pseudopodia extension, with inhibition escalating as the drug concentration raised. Cytoskeleton staining depicted in Fig. 4C illustrated striking disparities in cell cytoskeletal organization between untreated and MAD-treated groups. Untreated cells exhibited robust adhesion, distinct hierarchical structures, and extensive pseudopodia extension. However, at a moderate MAD concentration (0.25 μM), cells exhibited outwardly extending microfilaments, reduced cell area, and some shrinkages, indicating a stress response induced by MAD that altered the local cellular environment and inhibited pseudopodia growth. At a high MAD concentration (1 μM), cells displayed significant shrinkage and protrusion, weakened adhesion, smoother cell boundaries with fewer wrinkles, and potential detachment of cell membrane fragments.

For detailed insights into cell morphology, we employed SICM for high-resolution imaging of the cellular membrane *in vitro*, both in the presence and absence of MAD, as shown in Fig. 4D. An electric bias of typically 100 mV was applied to the cell culture dish, with a sensing nanopipette connected to a current amplifier and grounded. The scanning electron microscope (SEM) image of a nanopipette section presented in Fig. 4E showcases a nanopore with an inner diameter of approximately 70 nm from the side view. The current-voltage (IV) curves were recorded using the SICM system (Fig. 4E), with bias voltages ranging from -0.6 to $+0.6$ V, at a scan rate of 50 mV/s, to prevent

hydrolysis and reference electrode instability. Through the SICM topographical images in Fig. 4F and G, the cytoskeleton was visibly organized and well-defined in untreated cells, while MAD-treated cells exhibited disorganized and chaotic cytoskeletal arrangements. Enhanced color imaging was utilized to accentuate topographical changes based on height variations between adjacent pixels, depicting blue for lower regions and orange for higher areas. Untreated cells demonstrated an evenly distributed cytoskeleton protein network, with filamentous pseudopodia potentially connecting with neighboring cells. Under treatment of 0.25 μM MAD for 24 h, pseudopodia growth was partially restrained, resulting in external protrusions. With 1 μM MAD treatment, pseudopodia extensions nearly vanished, prompting cells to adopt a round shape with minimal interconnections, as cytoskeleton proteins aggregated at cell poles, indicating protein reorganization.

Simultaneous mapping of topography and surface charge distribution of MDA-MB-231 cells

Recent research has emphasized the significance of comprehending the interaction between membrane morphology and surface charge distribution [14]. The electrical properties of cells are intricately intertwined with their structural integrity and chemical composition, regulating multiple cellular activities like growth, differentiation, and apoptosis [24,25]. These properties are also crucial for disease identification, early diagnosis, and prevention, aiding in distinguishing between healthy and diseased states. Notably, the overabundance of negative charges on tumor cell membranes plays a pivotal role in aberrant signal transduction pathways, which can be disrupted by

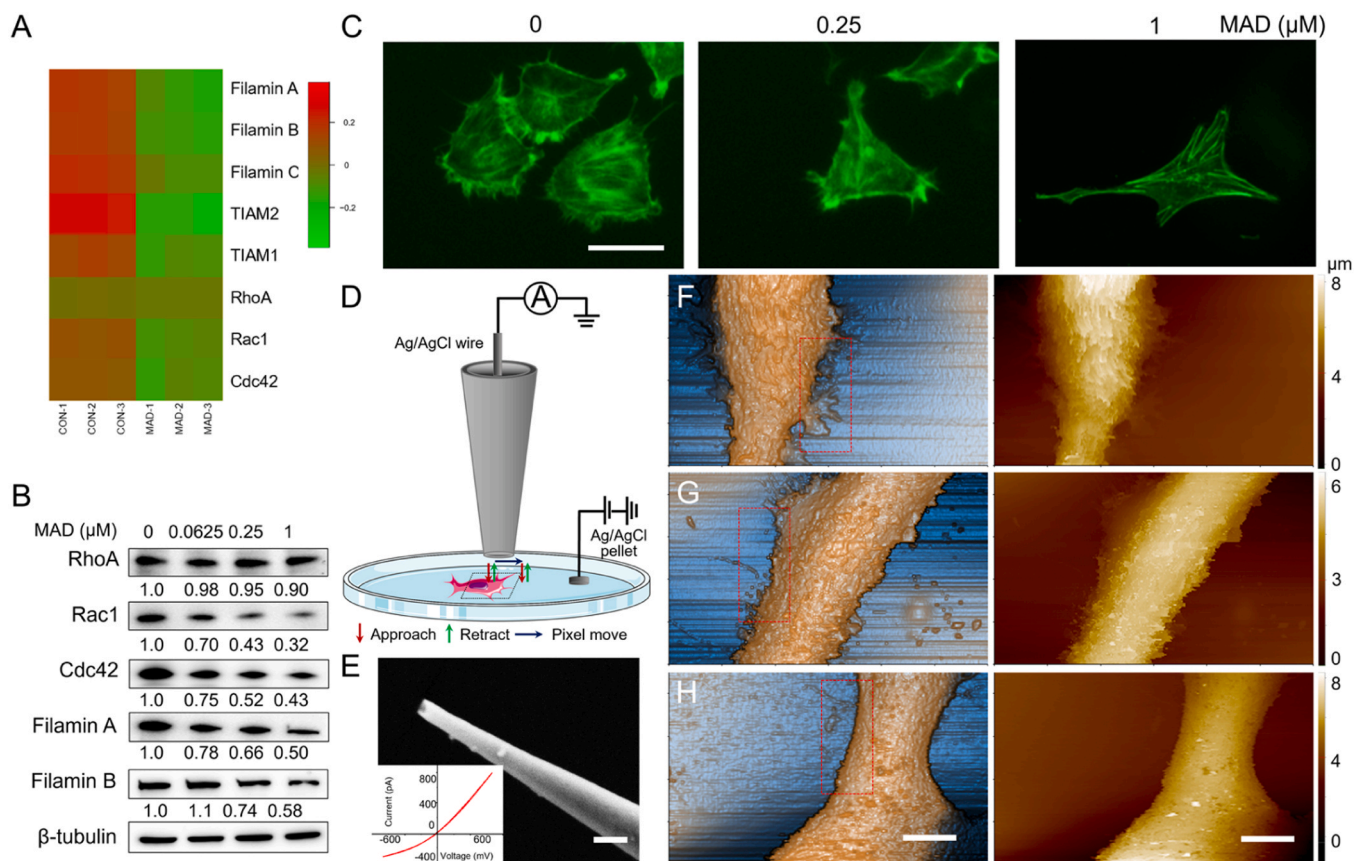


Fig. 4. Comparative analysis of cellular membrane morphology in MDA-MB-231 cells post-MAD treatment. (A) Heatmap analysis of pseudopod-related genes in the cytoskeleton following MAD treatment, based on transcriptome sequencing. (B) Western blot analysis of pseudopod-related protein expression. (C) Microscopic examination of pseudopod formation using phalloidin staining after MAD treatment (scar bar: 40 μm). (D) Schematic representation of the SICM experiment. (E) SEM image of a typical nanopipette alongside current-voltage (IV) curves measured using the SICM system. (F-H) Illustrative enhanced color images (left panel) and 2D images (right panel) depicting cell membrane topography observed through SICM (scar bar: 5 μm).

external environmental changes [26,27]. Here, we utilized a ΔI -SICM imaging method to examine the membrane topography and charge distribution of both untreated and MAD-treated MDA-MB-231 cells, as illustrated in Fig. 4A. To ensure precise scanning without lateral interference between the scanning probe and the scanned surface, the ARS (approach-retract-scan) and skip dual modes are commonly implemented, as previously reported [14]. Concisely, each pixel of the topography and ΔI image is captured after completing a full cycle (approach-pixel move-retract), as illustrated in Fig. 5B. During fine

scanning, the nanopipette is moved closer to the substrate starting from an initial position, D_{ps-max} , and then stops at D_{ps-min} once the current reduction surpasses a 2 % set-point. Subsequently, the nanopipette is retracted from D_{ps-min} back to D_{ps-max} . The ΔI value, calculated as the absolute difference between I_{ps-max} and I_{ps-min} , can reflect the surface charge difference.

The morphology and surface charge distribution within a $5 \times 5 \mu m^2$ area, illustrated in Fig. 5C-E, along with the average ΔI statistics in Fig. 5G, demonstrated that the cell membranes treated with 0.25 μM

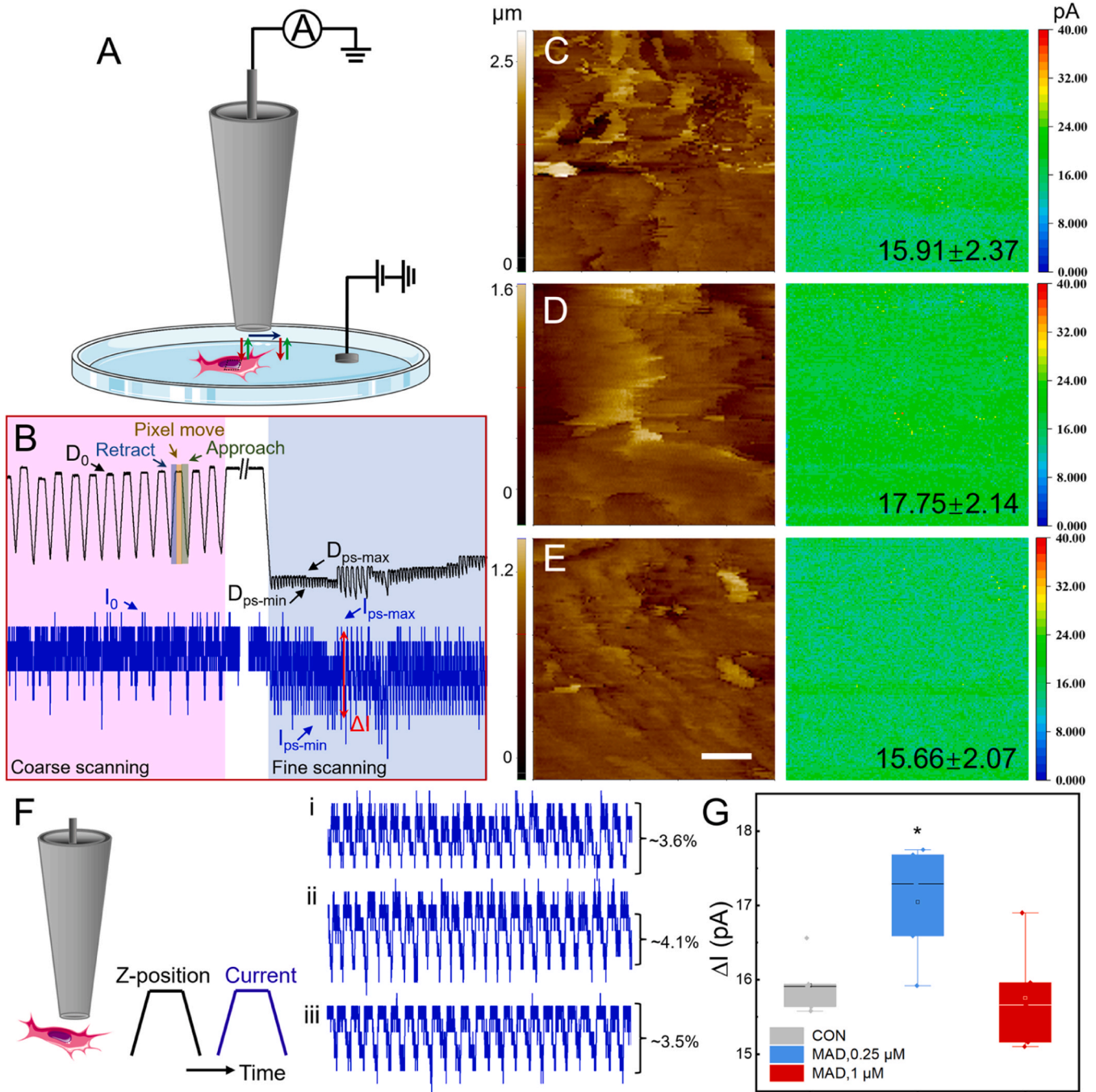


Fig. 5. Alterations in cell topography and surface charge in response to MAD treatments. (A) Schematic representation of the SICM experiment. (B) Tracking nanopipette movement and ionic current changes during scanning. Initial coarse scanning was followed by fine scanning with controlled D_{ps} (distance between the scanning probe and the sample). The nanopipette tip approached the sample from D_{ps-max} and halted at D_{ps-min} when the current reduction exceeded a predefined set-point (typically around 2 %). Simultaneous topography and surface charge imaging in control (C), 0.25 μM MAD (D), and 1 μM MAD (E) treatment conditions (scale bar: 1 μm). (F) Percentage decrease in current for control (i), 0.25 μM MAD (ii), and 1 μM MAD (iii) treatment. (G) ΔI values were obtained from the images of the control group and MAD-treated groups. * $P < 0.05$ vs control. (n = 5).

MAD for 24 h exhibited significantly higher negative charge compared to untreated cells. The nanopipette gradually approached towards the untreated cell until the current drop reached approximately 3.6 %. However, for cells treated with 0.25 μM and 1 μM MAD for 24 h, the nanopipette was advanced until current reductions of around 4.1 % and 3.5 % were achieved, respectively, as depicted in Fig. 5F. Regions exhibiting heightened ΔI values likely correspond to specific sites on the cell membrane where crucial proteins are concentrated, playing essential roles in processes such as the uptake of fatty acid and other cellular activities. Moreover, the surface charge of treated cells changes noticeably, indicating increased cell membrane permeability caused by 0.25 μM MAD. The MAD treatment may induce the composition and structural changes of cell membranes, and this heightened permeability and damage to the lipid bilayer could expose more negatively charged components, and the release of ions and other molecules may further disrupt the local electrostatic field [28]. At a higher concentration, the surface charge distribution tended to become more positive. This may be because at later stages of membrane damage, cells became fully permeable, and no large variations existed on the cell surface. These observations suggest underlying biochemical and bioelectrical alterations triggered by MAD treatment.

Figure S3A and B presented topographies and corresponding ΔI maps of living cells incubated with 0.25 μM MDA for 12 h and 48 h. The time course trend in ΔI can be summarized using the ΔI values obtained from these images, as shown in Figure S3C. After 12 h incubation, a

significant increase in ΔI was observed, accompanied by a broader dispersion interval. However, cells exhibited a stable response after 24 h, resulting in more consistent reactions over time.

Modulation of surface charge distribution by MAD via calcium channels

Calcium channels are integral components located on the cell membrane, capable of converting changes in membrane potential into transient fluctuations of intracellular calcium ions [29]. This process facilitates the influx of Ca^{2+} into the cell, subsequently triggering a cascade of downstream signaling pathways. Within the cell, Ca^{2+} serves as a crucial second messenger involved in vital physiological processes, including neuronal signal transmission, muscle contraction, gene expression, and cell development [30,31]. Notably, calcium signaling pathways are implicated in various pathological conditions, impacting processes like apoptosis, differentiation, metabolism, and gene transcription [32]. Dysregulation of Ca^{2+} flux is intricately linked to critical tumor progressions, such as proliferation, metastasis, migration, invasion, as well as resistance to anticancer drugs [33,34].

To explore the interplay between MAD's impact on cell invasion and calcium channels, comprehensive studies were conducted using ion channel chelators and agonists. Analysis of calcium channel-related gene expression shown in Fig. 6A revealed that MAD significantly suppressed these channels. Ethylenbis(oxyethylenetriol)tetraacetate (EGTA) is a well-known calcium ion chelator that specifically binds to

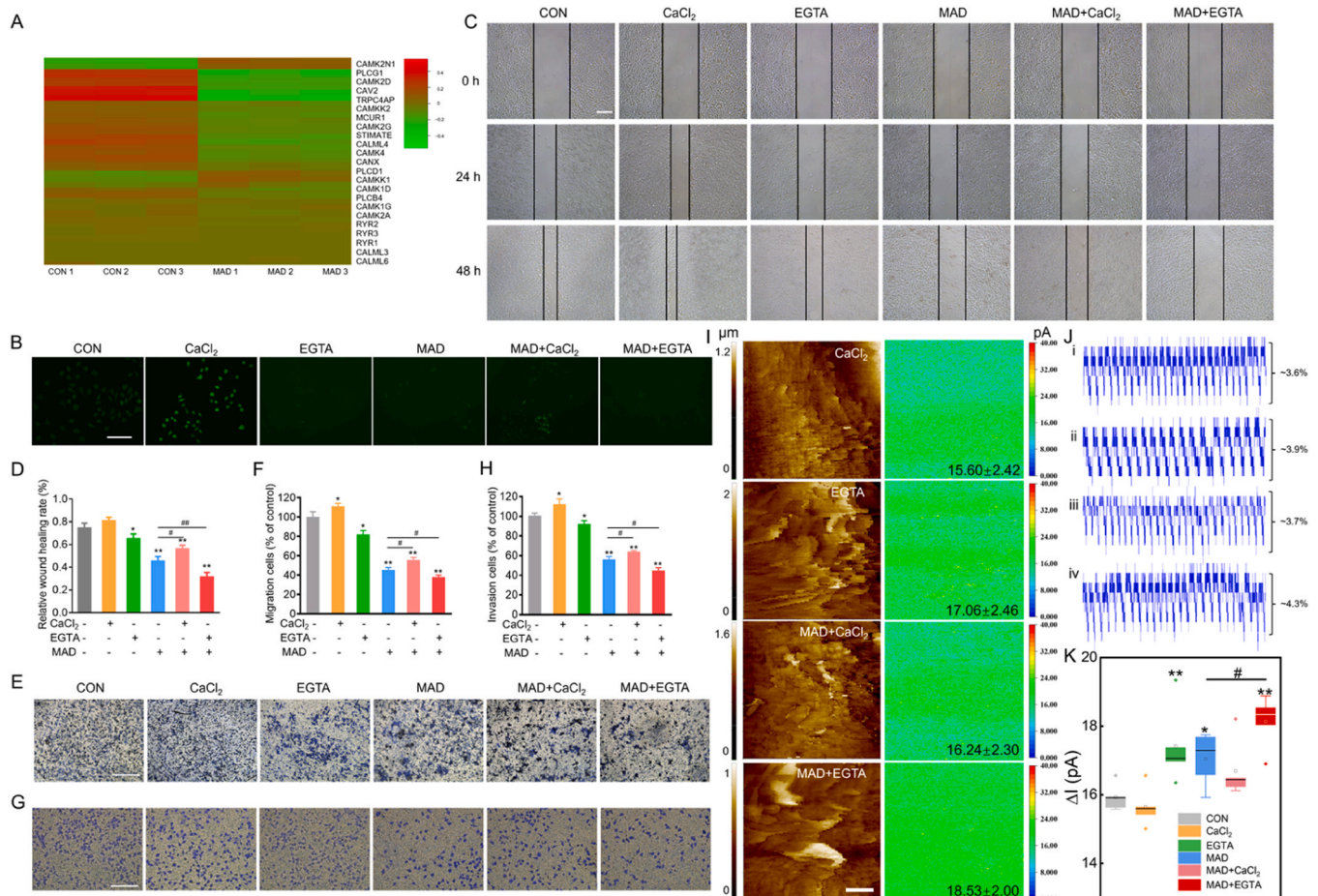


Fig. 6. Modulation of surface charge distribution by MAD via calcium channels. (A) Heatmap analysis of calcium channel genes assessed through transcriptome sequencing. (B) Evaluation of fluorescence intensity changes under different treatments using calcium ion probes (scale bar: 200 μm). (C-D) Scratch assay for assessing cell migration with different treatments (scale bar: 100 μm). (E-H) Transwell assay to detect the effects on cell migration and invasion under various treatments (scale bar: 200 μm). (I) Simultaneous topography and surface charge images under CaCl_2 , EGTA, MAD, MAD+ CaCl_2 , and MAD+EGTA treatment conditions (scale bar: 1 μm). (J) Percentage of current decrease for CaCl_2 (i), EGTA (ii), MAD+ CaCl_2 (iii), and MAD+EGTA (iv) treatment. (K) ΔI values were obtained from the images of treated groups (I). * $P < 0.05$, ** $P < 0.01$ vs control; # $P < 0.05$, ## $P < 0.01$ vs MAD. (n = 5).

Ca^{2+} , forming stable complexes that reduce intracellular free calcium concentrations, thereby restraining calcium-dependent biological processes [35]. Conversely, CaCl_2 serves as an external source of Ca^{2+} , elevating intracellular calcium levels and activating calcium signaling pathways. Fig. 6B showed a marked increase in Ca^{2+} fluorescence intensity in the CaCl_2 treatment group, indicating elevated intracellular Ca^{2+} levels, while the EGTA group exhibited a reduction in Ca^{2+} influx. Notably, MAD's effects were like those of EGTA, suggesting that MAD inhibited calcium channels and thereby modulated intracellular Ca^{2+} levels. Importantly, MAD significantly inhibited the MDA-MB-231 cells' ability to migrate and invade, with its action mechanisms partially linked to the suppression of calcium channels (Fig. 6C-H). Compared with the control group, both MAD and EGTA markedly impaired the cell capabilities to migrate and invade, underscoring the critical role of Ca^{2+} and highlighting MAD's effectiveness in inhibiting the activity of calcium channels. In contrast, CaCl_2 prominently enhanced cell migration, reinforcing the pivotal stimulatory role of Ca^{2+} in this process. Remarkably, even when co-administered with CaCl_2 , MAD's inhibitory effects persisted, albeit to a reduced extent, indicating that MAD can partially mitigate the stimulatory effects of Ca^{2+} . The combined application of MAD and EGTA notably enhanced the inhibitory effects on migration and invasion, effectively curtailing cell movement by jointly reducing the availability of Ca^{2+} .

Fig. 6. I depicted the topographical and corresponding ΔI images of cells incubated with CaCl_2 , EGTA, MAD+ CaCl_2 , and MAD+EGTA, showcasing distinct cellular responses. The ΔI values of CaCl_2 -treated cells were slightly less negative compared to untreated cells, while the EGTA and MAD treatments produced more negative surface charge distributions. Additionally, the inhibitory impact of MAD on calcium channels could be reversed by the addition of CaCl_2 , as significant ΔI changes in cellular behavior were noted in the MAD+EGTA group. In cells treated with MAD+ CaCl_2 and MAD+EGTA, the nanopipette was advanced until the current reductions of approximately 3.7 % and 4.3 % were achieved, respectively, as depicted in Fig. 6J. In conclusion, MAD demonstrated considerable promise as a therapeutic agent for breast cancer, particularly through its ability to modulate calcium ion channels and inhibit migration and invasion.

Conclusion

The electrical properties of cells are vital for determining their physiological state and serve as key indicators of health or disease. Various methods utilized to evaluate the electrical characteristics of cellular membranes have consistently revealed distinct differences between cancerous and normal cells. Understanding these disparities provides valuable perspective on the mechanisms underlying tumorigenesis and assists in identifying potential therapeutic targets. This study underscores the significant impact of maduramicin (MAD) in effectively restraining pseudopodia protrusion in tumor cells. By suppressing calcium channel activity, MAD alters the surface charge distribution and influences cellular migration. Ultimately, the intricate relationship between nanomembrane charge distribution and cellular functions highlights the innovative potential of therapeutic strategies designed to disrupt cancer cell behavior. Targeting these electrical properties may pave new avenues for cancer treatment, offering promising strategies to mitigate tumor invasiveness and improve patient outcomes.

Materials and methods

Materials and buffer solutions

Maduramicin (MAD, 92.3 %) was obtained from the China Institute of Veterinary Drug Control (Beijing, China). All other chemicals were purchased from Sigma Aldrich unless stated otherwise.

Diffusion, migration, and invasion assays in vitro and in vivo

Details of the diffusion, migration, and invasion assays were presented in the [supporting information](#).

Transcriptome analysis

When MDA-MB-231 cells reached 70 % confluency, they were treated with 0.25 μM MAD for 48 h. Total RNA was then extracted from each group, which included three biological replicates, resulting in six samples analyzed using transcriptome sequencing technology. The transcriptome sequencing services were provided by Shanghai Lingen Biotechnology Co., Ltd.

ΔI -SICM instrumentation

A modified SICM (N12, Park Systems) is customized for topography and surface charge measurements. Initially, we prepared quartz theta capillaries (BF100–58–15, Sutter Instrument) by cleaning them using a piranha solution, followed by three rinses with DI water. Nanopipettes were fabricated using a P-2000G laser probe puller with the following pulling parameters: HEAT= 275; FIL= 4; VEL= 50; DEL= 225; and PUL= 150. The nanopipette was employed to regulate the probe-sample distance (D_{ps}) via ionic current sensing, which was gauged by a current amplifier.

Living cell SICM imaging

Cells were allowed to adhere to the fibronectin-coated-PDMS substrates, which are transparent and enable bright field optical microscope imaging to guide the position of the scanning probe [36]. The cells were seeded at low confluency to facilitate single-cell scanning and living cell ΔI -SICM experiments were conducted in α -MEM media at 37 °C. The SICM imaging operates as reported previously [14]. In brief, the modified ΔI -SICM system first conducted a coarse scan (typically with 64 or 32 pixels) to assess overall height variation, followed by a fine scan (typically with 256 or 128 pixels).

CRediT authorship contribution statement

Jiang Shanxiang: Software. **Chen Feng:** Writing – review & editing, Validation, Supervision, Funding acquisition, Conceptualization. **Gu Ning:** Validation, Supervision, Resources. **Guo Dawei:** Writing – review & editing, Validation, Supervision, Funding acquisition, Conceptualization. **Jin Juan:** Investigation. **Sun Jingjing:** Software. **Duan Genhua:** Visualization. **Gao Xiuge:** Methodology. **Song Yao:** Writing – original draft, Methodology, Investigation, Formal analysis. **Lin Mengjuan:** Software, Methodology, Data curation. **Wang Moran:** Software, Investigation. **Jia Tianqi:** Software, Investigation. **Song Xinhao:** Writing – original draft, Software, Methodology, Investigation, Data curation, Conceptualization.

Declaration of Competing Interest

The authors declare no competing financial interest.

Acknowledgments

This study was supported by the National Sciences Foundation of China (32172918), the Fundamental Research Funds for the Central Universities (KYCXJC2024002), the National Natural Science Innovative Research Group Project (61821002), the Frontier Fundamental Research Program of Jiangsu Province for Leading Technology (BK20222002), National Key R&D Program of China (2023YFF0713600), and Project Funded by the Priority Academic Program Development of Jiangsu Higher Education Institutions (PAPD).

Appendix A. Supporting information

Supplementary data associated with this article can be found in the online version at [doi:10.1016/j.nantod.2025.102774](https://doi.org/10.1016/j.nantod.2025.102774).

Data Availability

Data will be made available on request.

References

- [1] E. Nolan, G.J. Lindeman, J.E. Visvader, *Cell* 186 (2023) 1708–1728.
- [2] M. Amgad, J.M. Hodge, M.A.T. Elsebaie, C. Bodelon, S. Puvanesarajah, D. A. Gutman, K.P. Siziopikou, J.A. Goldstein, M.M. Gaudet, L.R. Teras, L.A. D. Cooper, *Nat. Med.* 30 (2023) 85–97.
- [3] L.A. Korde, M.R. Somerfield, L.A. Carey, J.R. Crews, N. Denduluri, E.S. Hwang, S. A. Khan, S. Loibl, E.A. Morris, A. Perez, M.M. Regan, P.A. Spears, P.K. Sudheendra, W.F. Symmans, R.L. Yung, B.E. Harvey, D.L. Hershman, *J. Clin. Oncol.* 39 (2021) 1485–1505.
- [4] R. Moreddu, *Adv. Sci.* 11 (2023).
- [5] T. Banerjee, D. Biswas, D.S. Pal, Y. Miao, P.A. Iglesias, P.N. Devreotes, *Nat. Cell Biol.* 24 (2022) 1499–1515.
- [6] N.M. Goldenberg, B.E. Steinberg, *Cancer Res.* 70 (2010) 1277–1280.
- [7] J.A. Moleón Baca, A. Ontiveros Ortega, A. Aránega Jiménez, S. Granados Principal, *Bioelectrochemistry* 144 (2022).
- [8] S.M. Leitao, B. Drake, K. Pinjusic, X. Pierrat, V. Navikas, A.P. Nievergelt, C. Brillard, D. Djekic, A. Radenovic, A. Persat, D.B. Constam, J. Anders, G. E. Fantner, *ACS Nano* 15 (2021) 17613–17622.
- [9] C. Zhu, K. Huang, N.P. Siepser, L.A. Baker, *Chem. Rev.* 121 (2021) 11726–11768.
- [10] P. Novak, A. Shevchuk, P. Ruenaroengsak, M. Miragoli, A.J. Thorley, D. Klenerman, M.J. Lab, T.D. Tetley, J. Gorelik, Y.E. Korchev, *Nano Lett.* 14 (2014) 1202–1207.
- [11] V. Navikas, S.M. Leitao, K.S. Grussmayer, A. Descloux, B. Drake, K. Yserentant, P. Werther, D.P. Herten, R. Wombacher, A. Radenovic, G.E. Fantner, *Nat. Commun.* 12 (2021) 4565.
- [12] F. Chen, J. He, P. Manandhar, Y. Yang, P. Liu, N. Gu, *Nanoscale* 13 (2021) 19973–19984.
- [13] D. Perry, B. Paulose Nadappuram, D. Momotenko, P.D. Voyias, A. Page, G. Tripathi, B.G. Frenguelli, P.R. Unwin, *J. Am. Chem. Soc.* 138 (2016) 3152–3160.
- [14] Y. Song, S. Zhang, C. Cao, J. Yan, M. Li, X. Li, F. Chen, N. Gu, *Small Methods* (2023).
- [15] X. Song, Y. Zhang, R. Zuo, J. Zhang, M. Lin, J. Wang, S. Hu, H. Ji, L. Peng, Y. Lv, X. Gao, S. Jiang, D. Guo, *Int. J. Pharm.* 625 (2022).
- [16] H. Ming, B. Li, H. Tian, L. Zhou, J. Jiang, T. Zhang, L. Qiao, P. Wu, E.C. Nice, W. Zhang, W. He, C. Huang, H. Zhang, *Mater. Today Bio* 15 (2022).
- [17] Y. Sun, Y. Gu, X. Gao, X. Jin, M. Wink, F.S. Sharopov, L. Yang, G. Sethi, *Pharmacol. Res.* 195 (2023).
- [18] Y. Liang, H. Zhang, X. Song, Q. Yang, *Semin. Cancer Biol.* 60 (2020) 14–27.
- [19] S. Mittal, H. Kaur, N. Gautam, A.K. Mantha, *Biosens. Bioelectron.* 88 (2017) 217–231.
- [20] V. Padmanaban, I. Krol, Y. Suhail, B.M. Szczerba, N. Aceto, J.S. Bader, A.J. Ewald, *Nature* 573 (2019) 439–444.
- [21] I. Pastushenko, C. Blanpain, *Trends Cell Biol.* 29 (2019) 212–226.
- [22] R.W. A.D. Carlson, B.O. Anderson, H.J. Burstein, W.B. Carter, S.B. Edge, J.K. Erban, W.B. Farrar, A. Forero, S.H. Giordano, L.J. Goldstein, W.J. Gradishar, D.F. Hayes, C.A. Hudis, B.M. Ljung, D.A. Mankoff, P.K. Marcom, I.A. Mayer, B. McCormick, L. J. Pierce, E.C. Reed, J. Sachdev, M.L. Smith, G. Somlo, J.H. Ward, A.C. Wolff, R. Zellars, *J. Natl. Compr. Cancer Netw.: JNCCN* 9 (2) (2011) 136–222.
- [23] Y. Jiang, H. Zhang, J. Wang, Y. Liu, T. Luo, H. Hua, *J. Hematol. Oncol.* 15 (2022).
- [24] X.-K. Jin, K.-Q. Jin, X.-K. Yang, M.-Y. Wen, Y.-L. Liu, W.-H. Huang, *Anal. Bioanal. Chem.* 416 (2024) 4779–4787.
- [25] Y. Zhao, K.-Q. Jin, J.-D. Li, K.-K. Sheng, W.-H. Huang, Y.-L. Liu, *Adv. Mater.*, n/a 2305917.
- [26] N. Kanwar, K. Carmine-Simmen, R. Nair, C. Wang, S. Moghadas-Jafari, H. Blaser, D. Tran-Thanh, D. Wang, P. Wang, J. Wang, A. Pasculescu, A. Datti, T. Mak, J. D. Lewis, S.J. Done, *EBioMedicine* 52 (2020).
- [27] G.R. Monteith, N. Prevarskaya, S.J. Roberts-Thomson, *Nat. Rev. Cancer* 17 (2017) 373–380.
- [28] F. Chen, P. Manandhar, M.S. Ahmed, S. Chang, N. Panday, H. Zhang, J.H. Moon, J. He, *Macromol. Biosci.* 19 (2019) e1800271.
- [29] W.A. Catterall, *Cold Spring Harb. Perspect. Biol.* 3 (2011) a003947, a003947.
- [30] C. Giorgi, A. Danese, S. Missiroli, S. Patergnani, P. Pinton, *Trends Cell Biol.* 28 (2018) 258–273.
- [31] M.P. Young, Z.T. Schug, D.M. Booth, D.I. Yule, K. Mikoshiba, G. Hajnóczky, S. K. Joseph, *J. Biol. Chem.* 298 (2022).
- [32] I. Azimi, S.J. Roberts-Thomson, G.R. Monteith, *Br. J. Pharmacol.* 171 (2014) 945–960.
- [33] S. Zheng, X. Wang, D. Zhao, H. Liu, Y. Hu, *Trends Cell Biol.* 33 (2023) 312–323.
- [34] X. Shi, Y. Bi, W. Yang, X. Guo, Y. Jiang, C. Wan, L. Li, Y. Bai, J. Guo, Y. Wang, X. Chen, B. Wu, H. Sun, W. Liu, J. Wang, C. Xu, *Nature* 493 (2013) 111–115.
- [35] B. Xiang, G. Zhang, Y. Zhang, C. Wu, S. Joshi, A.J. Morris, J. Ware, S.S. Smyth, S. W. Whiteheart, Z. Li, *Arterioscler., Thromb., Vasc. Biol.* 41 (2021) 234–249.
- [36] Y.J. Chuah, S. Kuddannaya, M.H.A. Lee, Y. Zhang, Y. Kang, *Biomater. Sci.* 3 (2015) 383–390.